Cell Reports
Physical Science

CellPress

Article

Reversible photo-electrochemical device for solar hydrogen and power generation

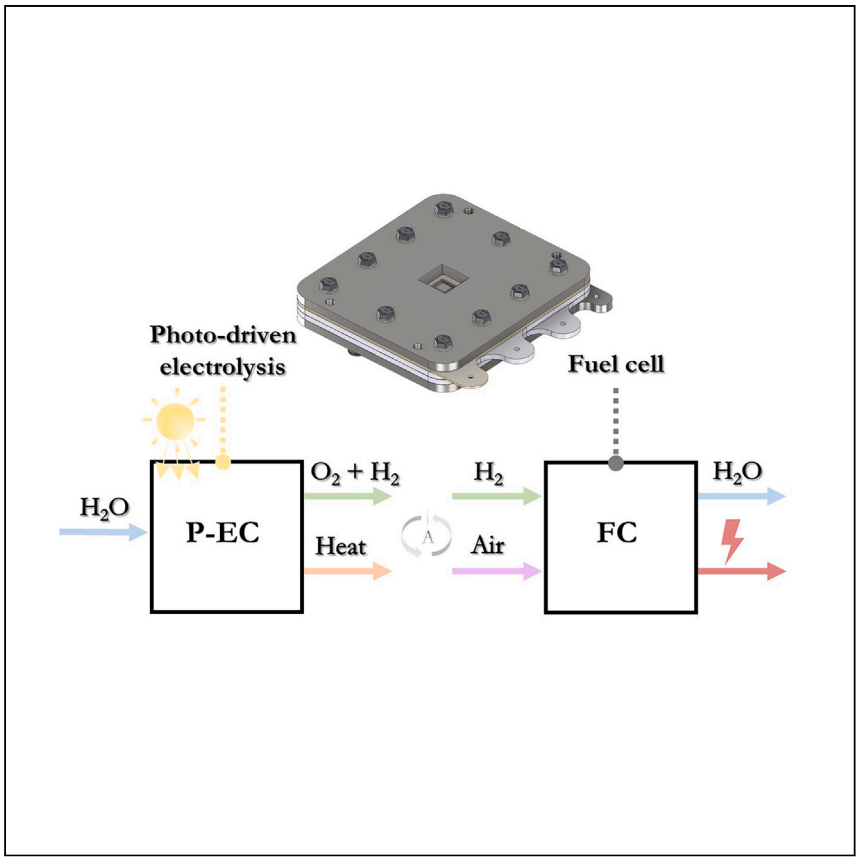

Patel et al. demonstrate the reversible operation of a photo-electrochemical device for both hydrogen and oxygen production in the photo-driven electrolysis mode and power generation in the fuel cell mode. This reversible process may contribute to solutions for stand-alone, solar-driven fuel and power production.

Mahendra Patel, Alexandre Cattry, Matthieu Jonin, Saurabh Tembhurne, Sophia Haussener

sophia.haussener@epfl.ch

Highlights

Reversible operation of a photo-electrochemical device operating with concentrated light

Device switches between electrolysis and fuel cell modes

Solar-to-hydrogen efficiency of 18.11% at 518 suns in photo-driven electrolysis (forward mode)

Stable power output of 35.7 mW/cm^2 as a fuel cell (reverse mode)

Patel et al., Cell Reports Physical Science 5, 101984
June 19, 2024
https://doi.org/10.1016/j.xcrp.2024.101984

Cell Reports
Physical Science

CellPress

Article

Reversible photo-electrochemical device for solar hydrogen and power generation

Mahendra Patel,[1,3] Alexandre Cattry,[1,3] Matthieu Jonin,[1] Saurabh Tembhurne,[1,2] and Sophia Haussener[1,4,*]

SUMMARY

A reversible photo-electrochemical device operating under concentrated irradiation could offer a stand-alone solution for producing solar fuel (in photo-driven electrolysis mode) and power (in fuel cell mode). This strategy would present the advantage of high mass-specific power density. Herein, we demonstrate such a reversible device in a fully automated and controlled experiment with a high-flux solar simulator, with concentrated solar irradiation ranging from 101 to 518 suns (i.e., 101 to 518 kW/m^2). In electrolysis mode, a solar-to-hydrogen efficiency of 18.11% and a current density of 292 mA/cm^2 are achieved at 518 suns with a device mass-specific power density of 6.76 W/kg. In fuel cell mode, a stable power density output of 35.7 mW/cm^2 at a 50 mA/cm^2 load and 48.2% voltage efficiency is achieved in constant gas configuration. Utilizing more permeable and hydrophobic gas diffusion layers on the cathode side of the fuel cell improves water removal and leads to an increase in power output by a factor of more than 2.5.

INTRODUCTION

Research on solar energy conversion into dense chemical fuel, such as H_2, aims to maximize efficiency and power density to enable cost-competitive, large-scale implementation. Technology development targets solar-to-hydrogen (STH) efficiencies exceeding 10%, large power output (>100 kW), substantial fuel production rates (>20 kg/day),[1] and low theoretical solar hydrogen production cost (<$2/kg H_2).[2,3] A comparison of experimental demonstrations of different solar fuel processing pathways[4] suggests that among the interesting candidates are thermally integrated photo-electrochemical devices operating under concentrated solar irradiation (termed concentrated integrated photoelectrochemical [CIPEC] devices).[5] Such CIPEC device demonstrations have reported STH efficiencies of 17%–20% and power outputs of 27 W to 2 kW.[6,7] CIPEC devices exploit controlled thermal management, minimize ohmic losses, but require an optical concentrator (allowing for high power density).[8] If such a CIPEC device could also be operated in the reverse direction, i.e., in fuel cell (FC) mode, it could possess unique advantages such as increased flexibility, compactness, and high specific energy and power density (Figure 1). These advantages are also interesting in the context of space applications, where energy density can become decisive, and where fuel and also oxygen (for life support), heat, and electricity are all desired products. Such reversible CIPEC devices can be classified as bifunctional (in analogy to unitized regenerative FCs [URFCs] powered by discrete photovoltaic [PV] panels or the electrical grid) and potentially provide economic, mass, and volume reduction benefits compared to the discrete electrochemical cell (EC) and FC-EC systems.[9] In contrast to dark URFCs, which have long been a subject

[1]Laboratory of Renewable Energy Science and Engineering, EPFL, Station 9, 1015 Lausanne, Switzerland

[2]SoHHytec SA, EPFL Innovation Park, Batiment C, 1015 Lausanne, Switzerland

[3]These authors contributed equally

[4]Lead contact

*Correspondence: sophia.haussener@epfl.ch

https://doi.org/10.1016/j.xcrp.2024.101984

Please cite this article in press as: Patel et al., Reversible photo-electrochemical device for solar hydrogen and power generation, Cell Reports Physical Science (2024), https://doi.org/10.1016/j.xcrp.2024.101984

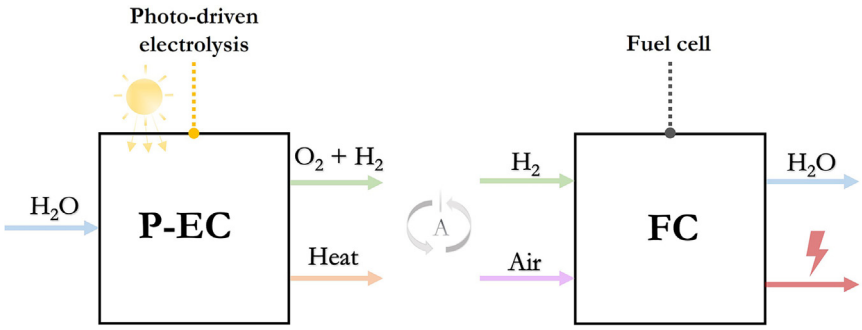

Figure 1. Schematic operation of the reversible CIPEC device

Solar-driven electrolysis mode (left) utilizing water and concentrated sunlight to produce hydrogen, oxygen, and heat (forward mode), and fuel cell mode (right) utilizing hydrogen and air to produce power and water (backward mode). P-EC, photo-driven electrolysis.

of study[10] and design optimization,[11] experimental demonstrations of reversible CIPEC devices do not exist. One major design challenge of the CIPEC is the requirement of simultaneous optimization of the photoabsorber (PA) and the reversible membrane-separated electrocatalyst. But this comes with the potential benefit of simplifying the peripherals (electrical wiring, DC-DC converter, etc.) and mitigating electrical losses in comparison to a URFC powered by separate PV panels.

One central aspect of achieving an operational reversible CIPEC device is the choice of catalysts.[12] Platinum (Pt) and iridium (Ir) are widely studied and considered state-of-the-art catalyst choices. While Pt most actively promotes the hydrogen oxidation reaction (HOR), oxygen reduction reaction (ORR), and hydrogen evolution reaction (HER),[13,14] Ir-based catalysts minimize activation overpotential losses for the oxygen evolution reaction (OER).[15] Thus, a combination of Pt and Ir, such as Pt-Ir mixture, seems to be an optimal choice for the air/water EC side, where Pt activates the ORR in FC mode, while Ir catalyzes the OER in electrolysis mode.[16–18] Pt is preferred for the electrolysis side, involving the HER in electrolysis mode and HOR during FC mode. For a reversible photo-driven electrolysis/FC device, additionally, we require information on the operational conditions in the photo-driven electrolysis mode, requiring *a priori* knowledge of the common operating point (voltage and current) of the integrated PA and electrolysis components. This information ensures that the chosen PA has a sufficient open-circuit voltage to sustain water electrolysis.[19] The operating point corresponds to the intersection of the PA and EC current-voltage (*I-U*) curves. The state-of-the-art PAs operating under concentrated light conditions use triple-junction PAs, as they provide high open-circuit voltage (>2.5 V at 1 kW/m^2 irradiation and >3 V at 100 kW/m^2 irradiation) capable of sustaining water electrolysis at high current density (>1 A/cm^2). These PAs typically have a small series resistance with a plateau region in the *I-U* characteristic of nearly constant current density. Sustaining the electrolysis of water in a potential range that is in this plateau results in the same performance (i.e., operating current density, STH efficiency) for Pt/Pt and Pt/Ir-Pt catalyst combinations. Whether in such a situation a Pt-Pt membrane electrode assembly (MEA) or a Pt/Ir-Pt MEA offers a more cost-competitive design for a given PA integrated in a CIPEC reversible device remains unclear. Conducting CIPEC experiments at high irradiation concentration is required to evaluate the operating conditions (i.e., water flow rate, irradiation concentration) at which one catalyst combination operates in the PA's *I-U* plateau region (i.e., total EC overpotentials kept below the PA maximum power point) or in the falling region (potential above the PA's maximum power point), the latter leading to a dramatic decrease of the device's STH efficiency if the irradiation concentration is further increased.

Please cite this article in press as: Patel et al., Reversible photo-electrochemical device for solar hydrogen and power generation, Cell Reports Physical Science (2024), https://doi.org/10.1016/j.xcrp.2024.101984

Another element crucial to the performance of the reversible CIPEC device is the coupled mass and charge transport in the device's components. This transport is affected by the gas diffusion layer's (GDL's) mesostructure (i.e., pore/fiber diameter and porosity, permeability, or effective conductivity[20]) and hydrophobicity, the water content of the ion-conducting membrane, and the geometry of the flow-field plates.

In contrast to a forward CIPEC device, the reversible CIPEC design requires a trade-off between the electrolysis and the FC-mode operational preferences. The performance of the CIPEC device is influenced by its EC flow-field plate design (e.g., serpentine or parallel channels), its channel height, and its channel-to-rib width ratio. In FC mode, smaller channel heights are essential to generate pressure drops that facilitate gas transport from the channel to the catalyst layer (CL).[21] However, in electrolysis mode, which operates with liquid water, increasing the channel height is preferred to reduce pressure drop and thereby mitigate the pumping power requirement. Moreover, higher electrical conductivity provided by low-porosity GDLs enables the electrolysis mode to operate more efficiently, minimizing ohmic overpotentials.[22] Conversely, efficient FC-mode operation requires permeable (by increasing the porosity and GDL pore size) and hydrophobic GDLs to ensure the removal of produced water, which otherwise obstructs reactant gases from reaching the catalyst surface. The use of hydrophobic carbon paper (e.g., Toray paper) as the GDL can enhance water removal; however, carbon corrosion during the OER prevents the use of such GDLs on the electrolysis-mode anode and requires the use of, for example, non-hydrophobic titanium (Ti)-based GDL. Alternatively, to overcome water accumulation in the CL, a microporous layer (MPL) coated with hydrophobic polytetrafluoroethylene (PTFE) and located between the CL and the GDL is utilized in state-of-the-art FCs.[23] The use of a PTFE-coated MPL has been shown not to be detrimental to the electrolysis-mode operation[24]; however, it has not yet been tested in the context of a reversible CIPEC device.

Here, we demonstrate the reversible operation of an automated stand-alone (i.e., peripherals are integrated to enable seamless switching between the electrolysis and the FC modes without manual intervention) constant gas configuration CIPEC device. The device operates with concentrated light (101–518 kW/m^2) in the photo-driven electrolysis mode. Two catalysts are investigated: (Pt-Pt) and (Pt-Pt/IrO_x). The performance of the FC mode in terms of power production is experimentally investigated by varying the hydrogen flow rates from 0.25 to 0.85 NL/min. Stable operating conditions for FC and photo-driven electrolysis modes are defined to predict CIPEC optimal operation enabling best water removal.[25] To overcome the low power output in the FC mode, we implemented the same water management strategies in the CIPEC device that are typically applied in URFCs (i.e., evaluating various GDLs with differing porosity and PTFE coating) and tested them in dark conditions. Such strategies, while existing for URFCs, have not yet been experimentally shown to work in CIPEC devices. The thereby generated experimental data are valuable for the validation of computational modeling of reversible CIPEC devices and provide an opportunity to explore thermal management strategies that could further improve the FC-mode operation (i.e., isolating and reusing generated heat in forward mode for increasing the FC operation efficiency).

RESULTS AND DISCUSSION

Performance characterization of the CPV and the reversible electrochemical cells

Initially, the performances of the concentrated PV (CPV) module and the electrochemical cell (with two different MEAs) were individually characterized. Figure 2A

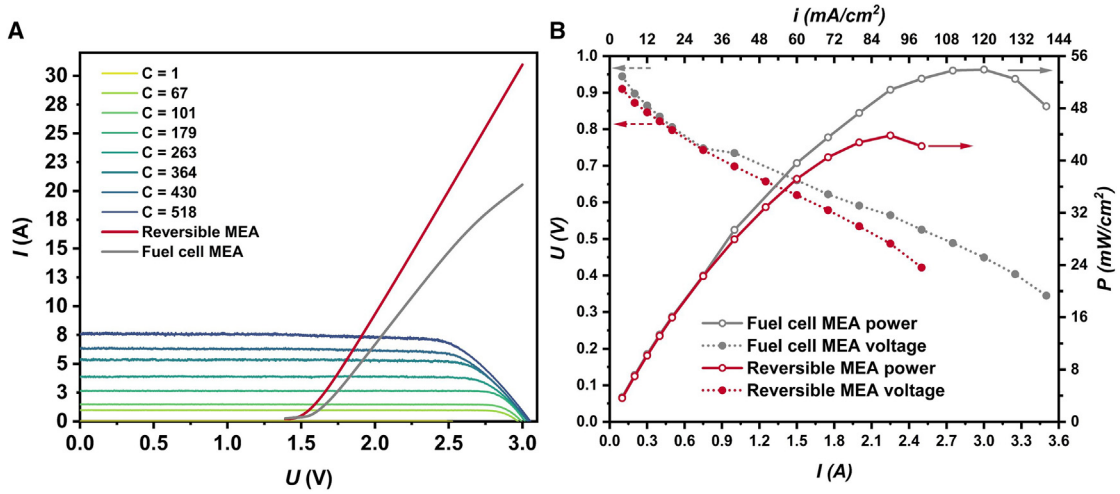

Figure 2. Individual performance of CPV module and electrochemical cell (in electrolysis and FC modes)

(A) *I-U* curves of the CPV module and two different MEA electrochemical cells, reversible MEA (with Pt/Pt catalysts, red) and fuel cell MEA (with Pt/Ir-Pt catalysts, gray). The CPV module's *I-U* characteristics were measured at various solar concentrations ranging between C = 1 and 518. The EC's *I-U* characteristics were measured with 20°C deionized water supplied from the cooling water bath. The performance characteristics of the CPV cell, including the fill factor, are shown in Table S3.

(B) Polarization and power density curves of two different MEA fuel cells, reversible MEA (red) and fuel cell MEA (gray), obtained at the beginning of the experimental campaign. Both measurements were conducted under the same ambient conditions. The open-circuit voltage for both curves was 1 V. The air and hydrogen flow rates were 2 and 0.85 NL/min, respectively.

shows the *I-U* characteristics of the triple-junction (GaInP/GaInAs/Ge) CPV module with an active area of 0.96 cm^2 and the electrochemical cell of 25 cm^2 with reversible and FC MEAs operated in the electrolysis mode. The PV performance of the CPV module (Figure S7 for a 0.96 cm^2 CPV area) was measured under the Trisol solar simulator normalized at 1 kW/m^2 (spectrum in Figure S11) and under concentrated irradiation in the high-flux solar simulator (HFSS). During the measurements, a water flow rate of 2–3.5 L/min was used to cool the CPV module. Deionized water was recycled and cooled down by the cooling water (bath maintained at 20°C) before being reinjected into the CIPEC module.

Increasing the irradiation concentration from C = 67 to 518 increases the photon flux arriving on the CPV cell, resulting in an increase of the short-circuit current density (I_{sc}) from 0.95 to 7.64 A (14.6 mA at 1 sun) and the open-circuit voltage from 3 to 3.05 V (2.55 V at 1 sun), giving an operating advantage at high current operation. By increasing the irradiation concentration, the water temperature (measured with a T_4 thermocouple) after the CPV cell increased from 24.6°C (C = 67) to 33.2°C (C = 518) because of the higher water absorption rate of the incoming photons in the infrared part of the light spectrum and convective heat transfer from the CPV module to the flowing water. Water absorption in the infrared part of the light spectrum is significant, with up to 63% water absorbance at a photon wavelength of 1,416 nm for a spacing between the quartz glass and the CPV module of 0.89 mm. Consequently, water absorption of the infrared light, while beneficial for heat management of the CPV module and electrochemical cell, reduces light absorption in the germanium (Ge) junction, which limits the last junction in terms of the photocurrent density (Note S3 and Figure S15). Therefore, the water channel was designed with a height not larger than 1 mm to ensure sufficient infrared light transmittance to the Ge junction.

The *I-U* characteristics of the electrochemical cell with Pt/Pt (referred to as FC MEA) or Pt/Ir-Pt (reversible MEA) MEAs were measured with a water flow rate of 2 L/min

and a water temperature of 21°C (measured with T_4 thermocouple) in dark electrolysis operation. The stoichiometric hydrogen molar flow rate was 0.018138 mmol/s for I = 3.5 A (i.e., the most significant current drawn from the FC during the experiments), corresponding to 0.02 L/min in FC operation. All reversible operation experiments used an over-stoichiometric hydrogen flow rate (0.85 NL/min). Although the Pt/Ir-Pt MEA more efficiently reduces activation overpotentials than the Pt/Pt MEA, with a 110 mV difference at 7.64 A (the highest current achieved in the experiment), both *I-U* curves (CPV and EC) intersect in the CPV's plateau region. The intersection of the CPV and electrochemical cell *I-U* characteristics corresponds to the CIPEC device's operating point at which hydrogen is produced. Both MEAs are, therefore, expected to generate the same hydrogen flow rate at the largest experimented CIPEC solar irradiation (i.e., up to 518 kW/m^2). The Pt/Ir-Pt MEA can be more favorably utilized if the operating current is higher, which can be achieved by increasing, for example, the irradiation concentration even further. The water temperature increase measured at the outlet of the top water channel (measured with T_4) has a beneficial effect on the MEA's performance by enhancing the catalytic activity and the membrane ionic conductivity. The effect of temperature on the MEA's *I-U* curve was assessed by varying the water bath temperature from 20°C to 50°C with a constant water flow rate of 2 L/min (Figure S5). At 10 A (i.e., 0.4 A/cm^2 when normalized by the EC area), the total overpotentials are reduced by 130 mV (from 20°C to 50°C) for both MEAs, which allows further increasing of the CIPEC operating current (by increasing the irradiation concentration) without decreasing the STH efficiency. This behavior occurs because the CPV and EC *I-U* curves intersect in the CPV's plateau region. In addition, water flow rates from 0.25 to 2 L/min at a temperature T_4 = 21°C were used to ensure that the electrolysis mode did not run into a mass-transfer-limited regime (Figure S6). Similar *I-U* curves were obtained for the two MEAs, indicating no mass-transfer limits of at least up to 2.5 V.

The FC mode performance of the electrochemical cell with the Pt/Ir-Pt and Pt/Pt MEAs was evaluated by recording initial polarization and power density curves, shown in Figure 2B (Note S4). The voltage was measured by varying the current, with a 0.1 A increment when $I \leq 0.5$ A and a 0.25 A increment when $I > 0.5$ A. At each step, the voltage was measured in steady-state conditions. The incremental current increase, which corresponds to an incremental reactant consumption rate increase, ensures that the CL is supplied with enough gaseous reactants during the load change. Both MEAs showed similar performance and could operate up to 1.5 A while maintaining a voltage higher than 0.6 V and avoiding produced liquid water accumulation in the GDL, ensuring safe FC operation and avoiding mass-transfer limits. However, incremental load increase is time-consuming (5–10 min to reach steady-state voltage for each applied current) and does not allow addressing applications requiring instant power demand. In that context, the dynamic response of the electrochemical cell was evaluated by loading from a low current (0.1 A) directly to higher currents (0.75, 1, 1.25, and 1.5 A). When the current is increased, the FC performance is transient initially, with two observable phases (Figure S16). During the first phase, the current increase leads to a higher oxygen/hydrogen consumption rate at the CL (Figure S17). The reactant depletion at the CL leads to a sudden voltage drop. Simultaneously, a reactant concentration gradient develops between the CL and the gas-flow channel. Consequently, gaseous reactants diffuse from the gas channel and replenish reactants within the CL. In the second phase, the membrane dehydrates as the current density increases and results in increasing ohmic overpotentials. As oxygen replenishes the CL, produced water fills the pores and obstructs gas transport within the Ti frit. The low permeability of the Ti frit exacerbates water flooding and therefore mass transport. At the same time, water diffuses from

Please cite this article in press as: Patel et al., Reversible photo-electrochemical device for solar hydrogen and power generation, Cell Reports Physical Science (2024), https://doi.org/10.1016/j.xcrp.2024.101984

the cathode to the anode, rehydrating the membrane and liberating the catalyst pores. The voltage subsequently increases until the steady-state regime is achieved.[26,27] However, if the current increases from 0.1 A directly to 1.5 A, transient gas starvation leads to a critical voltage drop and causes long-term degradation (e.g., corrosion of the anode carbon Pt support in hydrogen-starved conditions[28,29]). To avoid such a voltage drop, the current can be first increased to an intermediate current. Alternatively, the hydrogen flow rate can be increased at a flow rate larger than 0.25 NL/min to enhance the reactant diffusion rate from the convective channel to the CL during the load step increase (Figure S18).

Integrating multiple functionalities into a single device leads to design trade-offs. For operation up to 518 suns, the photo-driven electrolysis mode operates at its highest efficiency (i.e., in the CPV *I-U* plateau region), even when a less-efficient MEA (Pt/Pt vs. Pt/Ir-Pt) is utilized. This confirms that the FC operation is limiting, and sacrificing a bit on the electrolysis-mode performance is acceptable as it does not affect the STH efficiency, while in turn it improves the FC mode performance.

Reversible operation of the CIPEC device

To demonstrate the feasibility and reproducibility of the reversible CIPEC operation, six automated continuous cycles, alternating between the photo-driven electrolysis (15 and 10 min for the first four and last two cycles, respectively) and the FC modes (35 min), were conducted with the two different MEAs (Pt/Ir-Pt MEA or Pt/Pt MEA). During the first 5 min, the photo-driven electrolysis mode is in a transient regime, resulting from the HFSS's lamp's transient behavior when switched on. After 10 min in a steady-state regime (5 min for the last two irradiation concentrations), the HFSS's lamps are switched off, and the FC mode is automatically actioned through solenoid valves, which stop the water flow and start the air/hydrogen flow. Before going into the FC mode, a dark electrolysis step (5 min) is run to ensure the best mass-transfer conditions. The FC mode reaches, in steps of 0.1 A (for 10 min) and 1 A (for 15 min), a final charge of 1.25 A for 10 min, so that the FC mode is safely operated by mitigating potential damage during load change. At the end of the FC mode, the photo-driven electrolysis mode is automatically activated by switching on the HFSS's lamps and through solenoid valves, which stop the air/hydrogen flow and start the water flow.

The photo-driven electrolysis mode was operated under irradiation concentrations varying between 101 suns for the first cycle and 518 suns for the last cycle. The last two irradiation concentrations (C = 429 and 518) were more critical to operate, as the temperature of the CPV and water stream increased over time under high heat accumulation. The high heat accumulation can cause the quartz glass to break over time. Therefore, the operating time was reduced by 5 min. Steady-state operation of the HFSS was achieved 5 min after the lamps were switched on, which ensured 5 min of operation in steady state for the last two irradiation concentrations. The temperature of the water stream was measured at the inlet, at the outlet, and after cooling the PV module of the CIPEC device. Hydrogen mass flow-rate fluctuations of less than 1.5% at C = 518 around the averaged values with a standard deviation of 0.00032 mg/s were observed and are due to the fluctuations in the HFSS lamps (flickering of the arc), in agreement with reported observations by Tembhurne et al.[6] The transient temperature increase during the experiment did not affect the hydrogen production rate, as the CIPEC device operates in the plateau region of the *I-U* curves, i.e., at the best operating point. Indeed, the open-circuit voltage of the PA decreases with temperature increase, and it conversely rises with an increase in

Please cite this article in press as: Patel et al., Reversible photo-electrochemical device for solar hydrogen and power generation, Cell Reports Physical Science (2024), https://doi.org/10.1016/j.xcrp.2024.101984

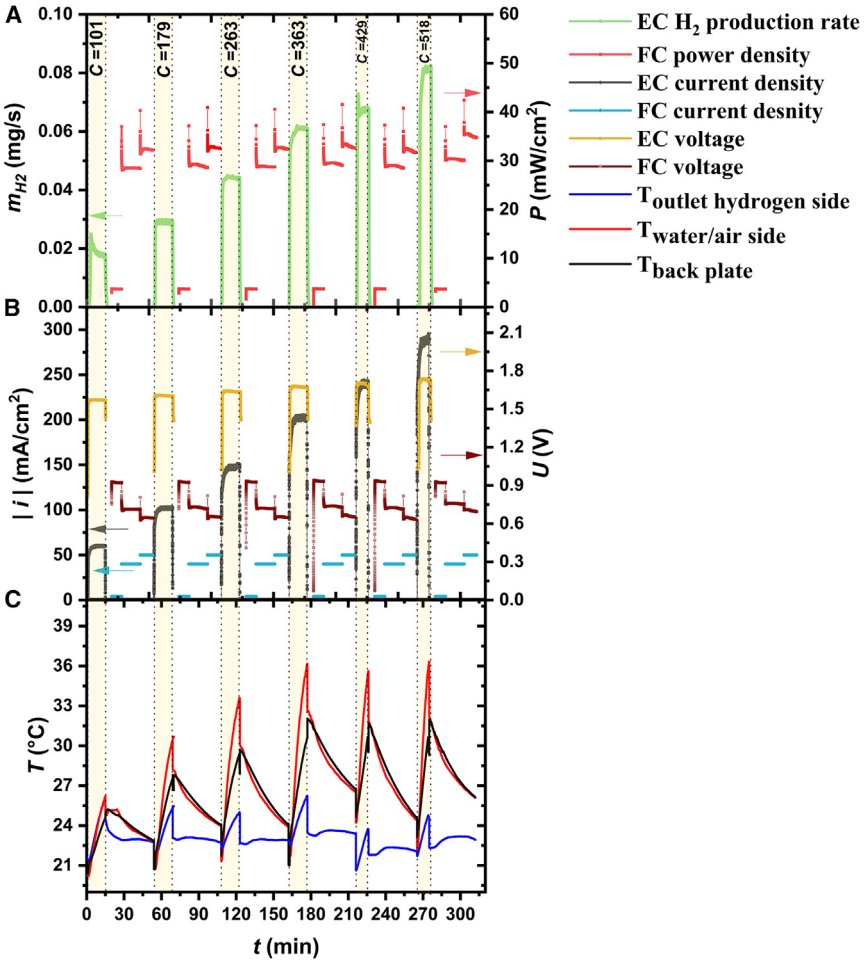

Figure 3. Reversible operation of the CIPEC device (with reversible MEA) for six consecutive cycles at different irradiation concentrations

Irradiation concentrations between 101 and 518 are shown. The photo-driven electrolysis mode (light yellow areas) and the fuel cell (FC) mode (white shades) are shown for an EC cell with Pt/Ir-Pt MEA (reversible MEA). (A) Hydrogen production rate in EC mode (green) and fuel cell power density in FC mode (pink); (B) current density (gray for EC mode and blue for FC mode) and operating voltage (yellow for EC mode and brown for FC mode); and (C) temperature profiles at the outlet hydrogen side (T3 in blue), inside the water/air side electrode (T4 in black), and at the back plate (T5 in red).

concentration, as shown in Figures 3B and 4B, and it is important to maintain efficient cooling throughout the solar-driven electrolysis operation. The operating water flow rate was 2 L/min; however, as excessive heat and local hotspots were observed (temperature increase, color change in epoxy) at the surface of the CPV module when the cooling flow rate was insufficient, the water flow rate was increased to 3 L/min for C = 429 and 3.5 L/min for C = 518. By increasing the water flow rate, the temperature peak at the cathode back plate decreased from 36°C in the fourth cycle (C = 363) to 35°C in the fifth cycle (C = 429) (Figures 3C and 4C), indicating that the overall device is more efficiently cooled down despite higher heat generation. The mean hydrogen flow rates were calculated by averaging the steady-state operation performance for each irradiation concentration starting 5 min after switching the lamps on. In FC-mode operation, steady-state operation at each load was ensured before switching to a higher load, which was achieved after ~5 min. The load at 1 A was

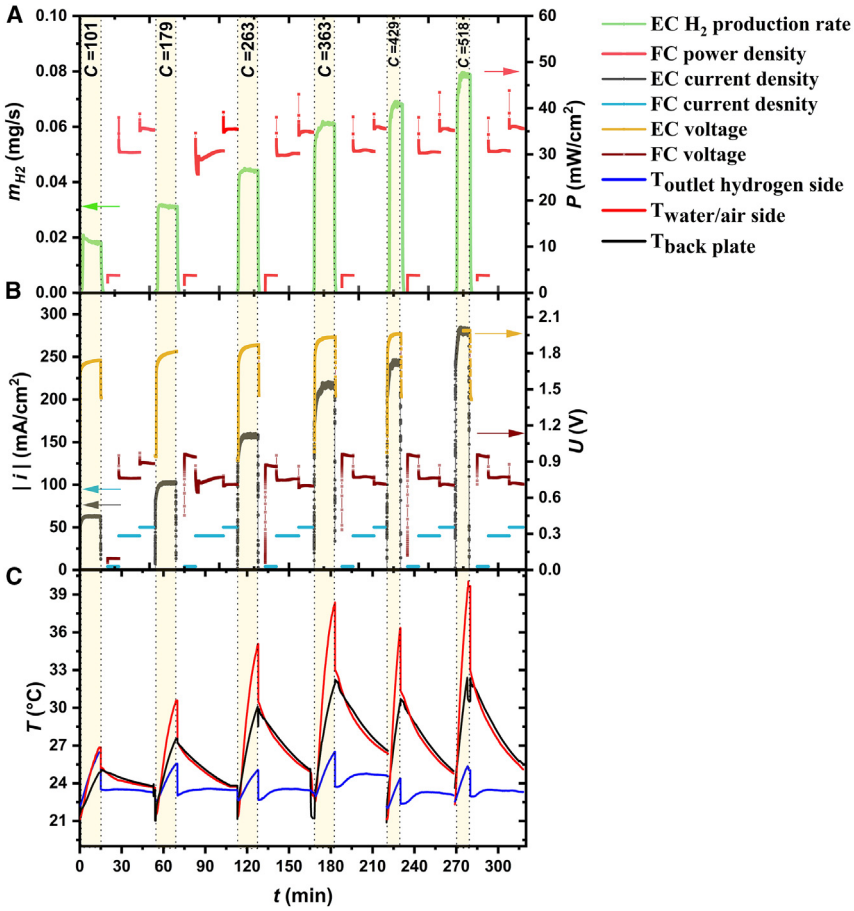

Figure 4. Reversible operation of the CIPEC device (with fuel cell MEA) for six consecutive cycles at different irradiation concentrations

Irradiation concentrations between 101 and 518 are shown. The photo-driven electrolysis mode (light yellow areas) and the fuel cell (FC) mode (white shades) are shown for an EC cell with Pt/Pt MEA (FC MEA). (A) Hydrogen production rate in EC mode (green) and fuel cell power density in FC mode (pink); (B) current density (gray for EC mode and blue for FC mode) and operating voltage (yellow for EC mode and brown for FC mode); and (C) temperature profiles at the outlet hydrogen side (T3 in blue), inside the water/air side electrode (T4 in black), and at the back plate (T5 in red).

prolonged to 15 min to ensure that operation at 1.25 A was stable and did not run into hydrogen-starvation operation due to too-rapid load increase. The FC power density was calculated by averaging the performance at steady state 5 min after each load increase, i.e., for 5 min at 0.1 A, 10 min for 1 A, and 5 min for 1.25 A.

Similar and stable performances in operating current density, hydrogen flow rate, and FC power output were observed for the six cycles with both Pt/Ir-Pt and Pt/Pt MEAs (Figures 3A and 4A). As predicted (see Figure 2A), the operating voltage in photo-driven electrolysis between devices with different MEAs differs by up to 260 mV at the highest irradiation concentration. This is attributed to higher activation overpotentials for the Pt/Pt MEA compared to the Pt/Ir-Pt MEA. At the largest irradiation concentration, i.e., $C = 518$, an average current density of 292 mA/cm^2, a stable operating voltage of 1.72 V (1.98 V for the Pt/Pt MEA), and a hydrogen flow rate of 0.08 mg/s were achieved, which were consistently stable in all photo-driven electrolysis and FC experiments. The results showed that, with increasing irradiation concentration, the photo-driven electrolysis current density increases

linearly with the number of suns, resulting in a hydrogen production rate ~518 times higher at 518 suns compared to 1 sun irradiation.

During photo-driven electrolysis mode, an STH efficiency of ~18.1% was calculated for all six irradiation concentrations. Hydrogen production rates were directly proportional to the irradiation concentration and were 0.081 mg/s at C = 518. At C = 518, the device output power based on the produced hydrogen was 9.7 W. The required pumping power for a water flow rate of 0.25–3.5 L/min was ~1%–~15% of this output power. During FC mode, the voltage efficiency ($= \frac{V_{measured,FC}}{1.48V}$, where 1.48 V is the thermoneutral voltage[30] for the FC mode) was calculated at different loads, with a maximum voltage efficiency of 62.5% ($V_{measured,FC}$ = 0.925 V) at 0.1 A, 52.0% (0.770 V) at 1 A, and 48.2% at 1.25 A (0.714 V). The efficiency at constant current operation is directly related to the power. The FC power density output increased from ~3.7 to ~35.7 mW/cm^2, with an intermediate power density of ~30.8 mW/cm^2 when increasing the load from 0.1 to 1 A and from 1 to 1.25 A. At 1.25 A, with a hydrogen flow rate of 0.85 L/min, the hydrogen fuel utilization rate was only 1%. The initial effect of the step load increase (e.g., from 0.1 to 1 A) is a reduction in power production, followed by a subsequent rise. This pattern arises from the fact that a sudden increase in the load causes a rapid consumption of reactants, creating a localized mass-transport limitation of the reactants. However, as diffusion from the channel to the CL restores the CL with reactant, this limitation is gradually alleviated, leading to the stabilization of the power output. While more challenging to achieve due to mass-transport limitations, increasing the load in FC mode results in increased power density output. The voltage efficiency decrease is attributed to current-dependent overpotentials, initial activation and ohmic losses, and, at higher currents, mass-transport losses (Figures 2B and S16). We observed a slight increase in the FC performance between the first and the last cycle, hypothesized to be the result of the thermal inertia that leads to increased temperatures (Figures 3C and 4C) and therefore also improved kinetics during the FC operation.

In the initial cycle at an illumination intensity of C = 101 suns, 10.8 mg of H_2 was accumulated in the final 10 min of steady-state operation with the HFSS. Subsequently, the FC mode operated with current values of 0.1 A for 10 min, 1 A for 15 min, and 1.25 A for 10 min, necessitating a stoichiometric hydrogen quantity of 17.27 mg. If our reversible system were to be operated in a closed system (i.e., with no other hydrogen, oxygen, or water source), the mismatch between the amounts of generated hydrogen and required hydrogen could be addressed by increasing either the irradiation concentration or the duration of the photo-driven electrolysis mode. At C = 263 suns, 26.4 mg of H_2 was accumulated in the last 10 min of the steady-state operation, exceeding the stoichiometric requirement for the FC mode. At C = 518 suns, 24.3 mg of H_2 was accumulated over just 5 min.

To demonstrate the reproducible performance of the CIPEC device in reversible operation, three identical continuous cycles were conducted with the Pt/Pt MEA. The integrated photo-driven electrolysis mode (10 min) was operated at 179 suns, and the FC mode was operated by loading from 0.1 A (10 min) to 1 A (10 min) (Figure S3). In photo-driven electrolysis mode, a current density of 108 mA/cm^2 was achieved for all three cycles, with a hydrogen production rate of 0.03 mg/s and a voltage of 1.77 V (Figure S4) in the steady-state regime. In FC mode, a power density of ~3.7 mW/cm^2 (0.1 A) and ~30 mW/cm^2 (1 A) was measured in the steady-state regime. The reproducible performance shows negligible CIPEC device degradation over the three different cycles.

Please cite this article in press as: Patel et al., Reversible photo-electrochemical device for solar hydrogen and power generation, Cell Reports Physical Science (2024), https://doi.org/10.1016/j.xcrp.2024.101984

Overall, we have shown that the photo-driven electrolysis-mode operation is comparable to the state-of-the-art CIPEC device in terms of STH efficiency (18.1% vs. 17% in Tembhurne et al.[6]) and maximum achievable irradiation concentration (518 suns vs. 474 suns in Tembhurne et al.[6]). The maximum achieved electrocurrent density was 292 mA/cm_{EC}^2 (vs. 880 mA/cm_{EC}^2 in Tembhurne et al.[6]), as the PA area had been reduced by 4 in the framework of developing a new-generation CIPEC device (reduced gas leakage, faster device assembly). Here, we showed that the CIPEC device can operate in continuous automated reversible cycles. The reversible operation is reproducible and stable in photo-driven electrolysis and FC modes. We demonstrated that the reversible CIPEC device can perform with other membrane-separated electrocatalysts (Pt/Pt MEA) with performance similar to that of the state-of-the-art Pt/Ir-Pt MEA utilized in URFC devices. We operated at up to 518 suns in photoelectrolysis mode with a photocurrent density of up to 292 mA/cm^2 and in reverse with an FC power output of up to 35.7 mW/cm^2. The standard round-trip efficiency (RTE) is usually evaluated at 1 A/cm^2, which corresponds to a practical current density required for industrial applications. We achieved a current density of only 0.14 A/cm^2 in FC mode (see Figure 2B, with the Pt/Pt MEA at ambient temperature), with an RTE of 19.2%. The RTE at the stable current density measured during the reversible CIPEC operation (0.05 A/cm^2, i.e., 1.25 A/25 cm^2) corresponds to an RTE of 42.2% and 41.8% for the Pt/Pt and Pt/Ir-Pt MEA, respectively. Despite achieving a higher STH efficiency compared to previously reported values in P-EC water splitting,[4] the diminished RTE points to suboptimal operational and design parameters of the reversible CIPEC cell when used in FC mode. Contributing to this inefficiency are factors such as the large depth (2 mm) and width (2.5 mm) of the channels on the cathode side (in FC mode), the low porosity (LP) of the Ti frit (0.22), and the accumulation of water during FC-mode operation. These factors collectively pose potential obstacles to attaining enhanced power densities. While addressing the first concern would entail creating a new cell design, the latter issues could be addressed within the existing device configuration.

Water management is of paramount importance to enhance gas mass transport in the GDL and increase the device's current density. Further efforts targeting the optimization of the CIPEC device design (such as the porosity and permeability of the GDL,[31] hydrophobic PTFE coating,[32] and use of a MPL[33]) to create an efficient (i.e., with higher RTE) CIPEC reversible design suitable for long-term stand-alone energy-storage applications are required and discussed in the next section.

Dark reversible CIPEC device with improved water management

To improve mass transport and power density in reversible CIPEC FC-mode operation at ambient conditions (1 atm and 20°C–25°C), tests were performed with two different GDLs (Freudenberg and Toray) on the hydrogen side and different Ti-fiber-felt (Ti-felt) porosities on the air/water side by using the same CIPEC device. As the Pt/Ir-Pt MEA is state of the art for URFCs, it was utilized to test the different GDL combinations. The experiments were conducted in dark conditions (i.e., externally biased by the potentiostat for the electrolysis mode) to omit damaging the CPV during the extensive and repeated assembly-disassembly of the cell (see Table S4). To test the influence of gas relative humidity on the CIPEC device performance, water bath humidifiers were utilized on the inlets. The following relative humidities were tested on the air and hydrogen, respectively, 60%-0%, 60%-95%, and 80%-95% under over-stoichiometric flow rates of, respectively, 3 and 1 NL/min. Using over-stoichiometric flow rates prevents gas starvation conditions within the CL, which otherwise lead to carbon corrosion and irreversible damage (see Figure S18). The

Please cite this article in press as: Patel et al., Reversible photo-electrochemical device for solar hydrogen and power generation, Cell Reports Physical Science (2024), https://doi.org/10.1016/j.xcrp.2024.101984

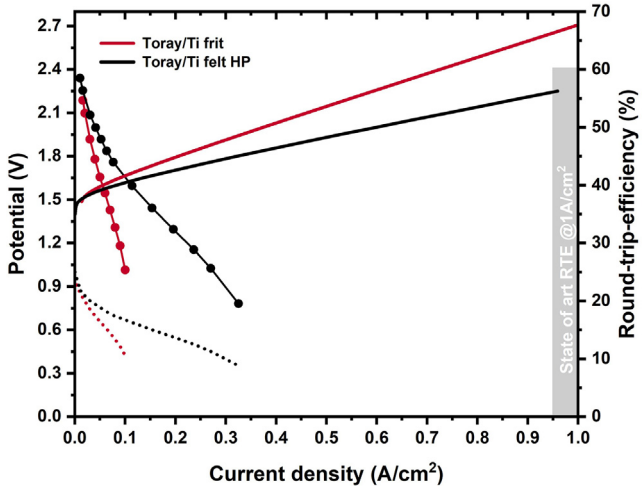

Figure 5. Performance of reversible CIPEC with two different GDLs

I-U characteristics (left) and RTE (right, solid line with dots) in electrolysis (solid) and FC (dotted) modes for the Pt/Ir-Pt MEA with initial GDL combination (Toray on hydrogen side and Ti frit on air/water side, red lines) compared to the optimal GDL combination (Toray on hydrogen side and Ti-felt HP on air/water side, black lines).

modified experimental setup is shown in Figure S20. In dark electrolysis mode, varying the flow rate from 0.25 to 2 L/min does not influence the EC *I-U* curve (Figure S6). Therefore, a constant water flow rate of 0.7 L/min was pumped from a water bath maintained at 20°C.

Figure 5 shows the *I-U* curves and RTE in electrolysis and FC modes for the initial GDL combination utilized for the reversible CIPEC demonstration (Toray on the hydrogen side and Ti frit on the air/water side) compared to the optimal identified GDL combination (Toray on the hydrogen side and Ti felt on the air/water side) tested in dark URFC mode (where the FC humidity conditions of the HFSS campaign were approximated by letting the humidity in the air side drop from 90% to 10% and to 0% in the hydrogen side). In addition, in the electrolysis mode, the device resistance with the Toray/Ti-felt combination was decreased by 0.41 Ωcm^2. This is due to fewer peripheral electrical connections and higher tightening torque (22–24 Nm) of the dark reversible CIPEC device. A higher torque was achievable due to the absence of damaging risks on the CPV.

Replacing the Ti-frit GDL (porosity 0.22, see Table S4) with a thinner and more porous Ti-felt GDL (Ti-felt high porosity [HP], porosity 0.74) enhances the FC-mode operation. The maximum achieved current density was 0.33 A/cm^2 before the potential dropped significantly due to mass-transport limitations (likely because the GDL is flooded with produced water). This is a 300% increase in the maximum obtainable current density compared to the initial GDL combination (Toray/Ti frit). The peak power density improved from 43.8 to 121.8 mA/cm^2, i.e., by a factor of 2.78. Increasing the porosity makes the GDL more permeable and enhances the evacuation of the produced water. Therefore, the mass transport from the catalyst is improved. Decreasing the thickness of the GDL also decreases the necessary travel path of water/air to and from the CL to the flow channels. In addition, the possibility of pore blocking by liquid water droplets is reduced, limiting water flooding. The RTE at 0.05 A/cm^2 increased from 41.8% to 48% when moving from the Ti frit to the Ti felt. A 1 A/cm^2 current density with an RTE of 60% is suggested to be industrially relevant for a URFC and state of the art in that field.[9] We assume a similar target would be relevant for our reversible CIPEC

device. System-level studies imply that even with RTEs of 30%, discrete EC/FC systems can be competitive with battery-based storage systems.[34]

To further mitigate water flooding, the GDL was coated with PTFE (a hydrophobic material).[35] While the water droplet contact angle was clearly increased (see Note S5 and Figures S23 and S24), the FC-mode operation with 5% PTFE coating was not improved compared to an uncoated GDL. It seems that, while PTFE enhances water removal, it also increases ohmic resistance. The improvement in the mass transfer is therefore counteracted by the increase in the device's electrical resistance, as shown in the electrolysis *I-U* curves for 0% PTFE and 5% PTFE (see Figure S25). Further investigations are required to validate this hypothesis.

The influence of humidifying the feeding gases was investigated for enhancing the electrical conductivity of the membrane. Figure S21 shows that, at lower current density operation, the FC power output is increased when humidifying the gases compared to a dry gas feed. The humidified gases mitigate the water flux from the membrane to the gas channels and consequently contribute to keeping an electronically conductive membrane. At higher current density, the water content in the humidified gas field increases as more water is produced. This leads to water saturation pressure and condensation, which eventually leads to flooding and voltage drop if this excess is not removed. At the same operating-current density, the dry-gas-fed system mitigates the water content in the GDL and mass transfer overpotentials, eventually producing higher power than the humidified-gas-fed operation. Therefore, humidifying the gas feed enhances the FC power output at low current density operation, while a dry gas feed increases the FC power output at higher current density.

The Toray/Ti-felt HP 5% PTFE was tested in URFC operation to characterize the operating current density and time under which the device is stable (Figure S22). As the maximum achievable current density is three times higher compared to the initial GDL combination tested in sun conditions (i.e., Toray/Ti frit, Figure 3), the FC power output was increased by three times (~91 mW/cm^2). At this current density, dry gas feed was utilized to prevent risks of GDL flooding. The FC power output was stable and maintained for 30 min over four consecutive cycles. EC parallel channels were designed for electrolysis-mode operation but performed poorly in FC mode. Smaller channels, smaller channel-to-rib ratio, and replacing parallel channels with more suitable serpentine ones are required to increase the pressure gradient over the gas-flow channel path.[21] This pressure drop enhances gas diffusion under the rib between two channels in the serpentine channels. The MEA area under the rib, therefore, contributes to producing power, limited in parallel flow channels. In addition, pressure drop enhances the fluid velocity and therefore accelerates droplet and humidity removal. This is advantageous in FC-mode operation but more detrimental in electrolysis operation. Indeed, more pumping power (see Note S6) is required for liquid water. A trade-off between the electrolysis and the FC modes is therefore required. Finally, increasing the temperature from ambient to 70°C–80°C is paramount to enhance catalyst activity and membrane conductivity. This is an advantage of reversible CIPEC devices, where solar power can be further used for maintaining the temperature in both electrolysis and FC modes by, e.g., heating specific component parts and/or reactants (gas or liquid) over their path inside the device.

This experimental campaign demonstrated the reversible operation of a CIPEC device. The CIPEC device operation in both forward mode (photo-driven electrolysis mode) and reverse mode (FC mode) under highly concentrated solar irradiation

Please cite this article in press as: Patel et al., Reversible photo-electrochemical device for solar hydrogen and power generation, Cell Reports Physical Science (2024), https://doi.org/10.1016/j.xcrp.2024.101984

(up to 518 suns) for two different MEAs (Pt/Ir-Pt MEA and Pt/Pt MEA) was experimentally shown. At 518 suns, a current density of 292 mA/cm^2 and an STH efficiency of 18.11% was recorded in the photo-driven electrolysis mode, while a stable FC power output of 35.7 mW/cm^2 under a 1.25 A load was maintained in the FC mode. The Pt/Pt and Pt/Ir-Pt MEAs showed similar performances in terms of current density, power density, hydrogen production rate, and operating voltage in both modes, as significant advantages are observable only at higher current density operation. Therefore, either MEA can be used in the CIPEC device design in small-scale applications.

While working on this demonstration, we encountered a variety of challenges, two of which are of general relevance: (1) complex fabrication of the device and (2) the need for optimized GDLs in terms of porosity, permeability, and PTFE coating so as not to be limited by mass transport in FC-mode operation and to achieve higher power densities. This first proof of concept, while not yet with record-breaking performance, shows that the CIPEC technology is extendable to the reversible-mode operation (making the CIPEC technology more versatile) and puts (reversible) CIPEC devices as an additional and alternative technology to the palette of solutions relevant for stand-alone renewable (solar) energy production units. Future efforts can target optimizing the CIPEC device design (GDL, EC anode channels) to create an efficient (i.e., with high RTEs) CIPEC reversible design achieving practical current density operation required for its industrial implementation. The FC-mode operation can be enhanced while minimizing the impact on the performance of the photo-driven electrolysis mode in reversible CIPEC operation. To assess the feasibility of compromising the performance of the photo-driven electrolysis without sacrificing efficiency, the MEA was changed. The substitution involved replacing the Pt/Pt-IrOx MEA (referred to as reversible MEA) with a Pt/Pt MEA (referred to as FC MEA), tailored for FC mode but less effective in electrolysis mode due to the increased activation overpotential in OER. Despite the shift in the EC *I-U* curve to the right caused by higher activation overpotential compared to the reversible MEA, the EC and PV *I-U* curves intersect at the plateau of the PV curve for irradiation concentrations up to 518 suns. Hence, the logical focus should be directed toward refining the FC-mode operation to enhance the overall performance of the reversible CIPEC cell without compromising its efficiency in photo-driven electrolysis under concentrated irradiation. We recommend the following actions to improve the CIPEC reversible operation: (1) smaller channel width, channel width-to-rib ratio, and channel height to increase gas pressure drop and gas diffusion under the rib connecting two channels to remove liquid water; a trade-off with increased pumping power in electrolysis mode should be investigated; (2) replacing FC cathode parallel channels with serpentine or interdigitated design, for which, however, the pressure drop is enhanced; and (3) implementing a recirculating water-heating loop to maintain the EC/FC part of the CIPEC device at 80°C, which will therefore enhance catalyst kinetics and electrical conductivity in both electrolysis and FC modes.

EXPERIMENTAL PROCEDURES

Resource availability

Lead contact

Requests for further information, resources, or materials should be directed to and will be fulfilled by the lead contact, Professor Sophia Haussener (sophia.haussener@epfl.ch).

Materials availability

This study did not generate new unique materials.

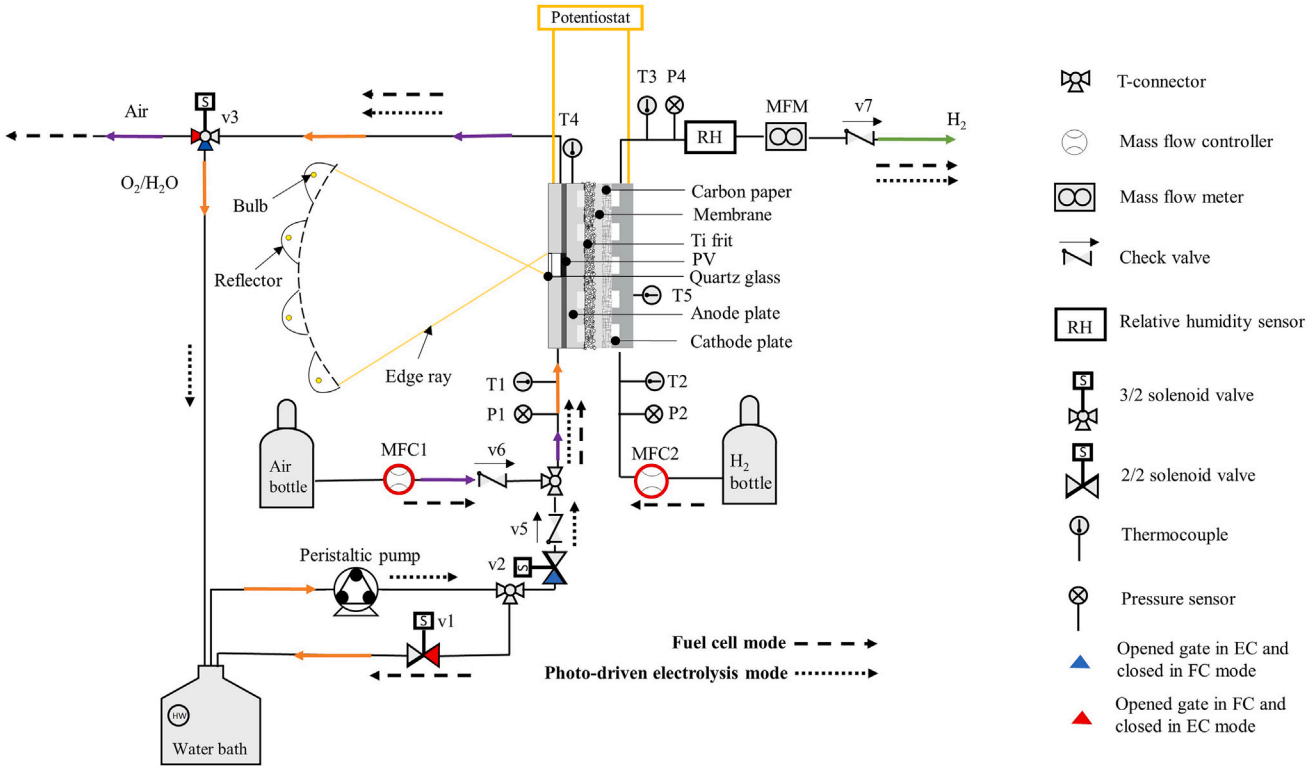

Figure 6. Experimental setup of the reversible CIPEC device operation in the HFSS
The purple, orange, and green arrows correspond to the air, water, and hydrogen streams.

Data and code availability

The data generated in this study are included in the article and supplemental information. The data in the main article are available at https://doi.org/10.5281/zenodo.10930988 and the data in the supplemental information will be made available from the lead contact upon reasonable request.

Experimental setup

The flow diagram of the experimental setup of the reversible CIPEC device operating under concentrated light is shown in Figure 6. The reversible operation was performed in constant-gas configuration (see Note S1 and Figure S26). This configuration allows for more practical automatization of the device, where only one control valve is required to switch between electrolysis and FC modes and where water or oxygen is supplied to the same electrode (i.e., EC anode and FC cathode). Consequently, the idle time between mode switches is reduced and quick start-up between power and fuel production is enabled.

In photo-driven electrolysis mode, the CIPEC device was mounted in EPFL's HFSS[36] with incoming solar irradiation characterized during the HFSS calibration (see Note S3 and Table S2). Deionized water (ionic conductivity <0.5 μS/cm), used to avoid any ion contamination, first flowed on top of the integrated CPV module, which is the PA in the current design, absorbing the infrared part of the incoming solar irradiation and convectively cooling the PA, and was subsequently fed (pre-heated) to the EC anode. Water and produced oxygen, collected at the anode outlet, were then recirculated with a peristaltic pump to the temperature-controlled water bath where the oxygen was released to the atmosphere. On the cathode side, during the

Please cite this article in press as: Patel et al., Reversible photo-electrochemical device for solar hydrogen and power generation, Cell Reports Physical Science (2024), https://doi.org/10.1016/j.xcrp.2024.101984

photon-driven electrolysis mode (i.e., when the HFSS lamps were switched on), hydrogen was produced from the reduction of protons and subsequently diffused toward the outlet. The MFC2 mass-flow controller was closed, preventing hydrogen from flowing toward the inlet. A check valve (V7) prevented backflow and ensured that the mass flow meter (MFM) recorded solely the produced humid (relative humidity [RH] 100%) hydrogen mass flow rate. At the end of the HFSS operation (i.e., at the end of the photon-driven electrolysis-mode operation), the peristaltic pump was stopped, and solenoid valves V1 and V2 were switched on and off, respectively. After an idle time of 5 min, allowing the switch from the photo-driven electrolysis to the FC mode and removal of the remaining liquid water in the channel through water vapor dark electrolysis (see Note S2), constant air and hydrogen flow rates set on the mass flow controllers (MFC1 and MFC2) were supplied to the cathode and anode, respectively. The hydrogen produced during the photo-driven electrolysis was vented, and a hydrogen generator was employed instead of a hydrogen storage bottle to enhance safety in the HFSS. V3 was switched on to release oxygen-depleted air into the atmosphere. Constant currents were drawn from the potentiostat, the voltage was subsequently measured, and the power output was derived. Further explanations of instruments and materials are given in the following sections. Humidity was not controlled during the experimental campaign in the HFSS and was likely on average 60%-0% in the air and hydrogen side (in FC mode). For the dark experiments, humidifiers were added to the setup (Figure S20), and conditions comparable to the HFSS setup conditions were approximated by letting the humidity in the air side drop from 90% to 10% during the experiment.

CPV module fabrication

The multi-step fabrication process of the CPV module is illustrated in Figure S2 and follows previously reported procedures.[37] A 290 × 390 mm^2 copper plate with a 10 × 10.5 mm^2 stage at the center was utilized as the substrate to hold the CPV cell. Prior to module preparation, the copper plate underwent a thorough cleaning regimen. The copper plate was initially immersed in a 1% H_2SO_4 solution for 30 min to eliminate the oxide layer. Subsequently, the plate was cleaned using acetone and subjected to an ultrasonic bath with isopropanol (IPA). The CPV cell employed in this fabrication process had a photoactive area of 1 cm^2 and comprised triple-junction GaInP/GaInAs/Ge solar cells from Azur Space (3C44 type version MC/glass). The soldering of the CPV cell onto the copper stage was carried out under N_2-saturated conditions at 240°C for 1 min. To ensure electrical insulation and connection of the gold-coated aluminum foil to the negative sides of the CPV cell, a PTFE frame was affixed using a high-thermal-resistance epoxy (Loctite EA 9497). The curing process for the epoxy was performed at 80°C for 90 min in an open-air oven. A gold-coated 0.25-mm-thick aluminum foil (1 × 3 cm^2 rectangle shape) was glued to the PTFE frame for electrical connection to the cathode plate. The CPV cell and the gold-coated aluminum foils were connected using 25 μm gold wire bonding. A total of 100 wires were utilized for wire bonding, connecting each side of the 1 mm gold strip of the CPV solar cell. To protect the wire bonds, a black protective epoxy (EPO-TEK H740E-2) was applied in two steps, followed by curing at 80°C for 90 min in the oven. The CPV module was mechanically and electrically connected to the anode plate using stainless steel screws. Similarly, the electrical contact between the cathode plate and the negative side of the CPV module was established through the aluminum foil and wire bonding, which was later attached to the Ti plate as a current collector.

Design and fabrication of the CIPEC device

The custom-made CIPEC device was made using different metal plates and gaskets stacked together, as illustrated in Figure S1. The CIPEC device consists of a directly

integrated CPV module and a zero-gap EC cell. The anode plate was made of Ti (grade 2), while the cathode plate was made of standard stainless steel. To facilitate efficient transportation of charge from the back side of the CPV module to the anode plate, the CPV module was mounted at the center of the anode plate and fabricated using copper material, known for its high electrical conductivity. Similarly, aluminum foils were employed to transport photo-generated electrons from the front side of the CPV module to the cathode plate. To ensure proper electrical isolation between the PV anode and the cathode plates, an ethylene propylene diene monomer (EPDM) gasket was placed on top of the anode plate. Furthermore, an additional EPDM gasket was incorporated into the stack to create a well-defined water-flow channel above the CPV module. This channel allowed for convective cooling of the CPV module, simultaneously increasing the water temperature. The water channel was directly connected to the anodic channels, enabling the pre-heated water to flow into the EC cell. The device was assembled with a Ti plate used as the back plate and a stainless-steel plate used as the front plate. The front plate featured a 2-mm-thick quartz glass window, securely attached with high-thermal-resistance epoxy. The window was designed at a 45° angle to enable concentrated light from the HFSS to reach the CPV module effectively. The device was screwed with stainless steel screws with a symmetric distribution of 10 N·m torque isolated with a cable shrink.

Materials

A commercially available reversible FC membrane (Fuel Cell Store) and hydrogen-oxygen FC membrane (Fuel Cell Store) were used for all the integrated and dark tests. The reversible FC membrane was 125 μm thick (Nafion 115) with an anode (in the electrolysis mode, cathode in the FC mode) catalyst coating of 1.5 mg/cm^2 of Ir-ruthenium oxide and Pt black each and a cathode (in the electrolysis mode, anode in the FC mode) catalyst of 3.0 mg/cm^2 Pt black. The hydrogen-oxygen FC membrane was 125 μm thick (Nafion 115) with an anode (in the electrolysis mode, cathode in the FC mode) catalyst coating of 4.0 mg/cm^2 of Pt black and a cathode (in the electrolysis mode, anode in the FC mode) catalyst of 4.0 mg/cm^2 of Pt black. A 1-mm-thick and porous (LP: 0.217) Ti frit was used as a GDL on the anode (in the electrolysis mode and cathode in the FC mode) side and porous (HP: 0.78) Toray paper 5% wt (Fuel Cell Store) on the cathode (in the electrolysis mode, anode in the FC mode) side. The porosity of the porous Ti frit and Toray paper was calculated by determining the mass and volume of the material and incorporating the bulk density and weight. In FC mode, high-purity air (ALPHAGAZ; synth air $\geq$ 99.999% vol abs) was used at the cathode, whereas in the anode, hydrogen was supplied from a hydrogen generator (LNI SWISSGAS; hydrogen purity $\geq$ 99.9999%). K- and T-type thermocouples were utilized to measure the temperatures at five locations: T_1 (at the water/air side inlet), T_2 (at the hydrogen side inlet), T_3 (at the hydrogen side outlet), T_4 (inserted inside the water/air side electrode), and T_5 (inserted at the back plate).

CPV characterization

The *I-U* characteristics of the CPV module were measured under the irradiation of an AM 1.5G solar simulator (OAI's TRI-SOL solar simulator 1–1.6 kW) with an intensity of 1 sun (1,000 W m^{-2}). The measurements were recorded using a Biologic VSP-300 potentiostat controlled by the EC-lab software. At higher concentrations, the *I-U* characteristics of the CPV module were measured with the assembled cell in the HFSS. The measurements were recorded using a Biologic HCP803 potentiostat with a (up to 80 A) booster.

Please cite this article in press as: Patel et al., Reversible photo-electrochemical device for solar hydrogen and power generation, Cell Reports Physical Science (2024), https://doi.org/10.1016/j.xcrp.2024.101984

Dark electrochemical characterization

All the dark electrochemical measurements were performed using the Biologic HCP803 potentiostat with a (up to 80 A) booster and controlled by the EC-lab software. All the dark experiments were conducted in a two-electrode setup.

Automatization of reversible operation

The solenoid valves were controlled remotely, as the HFSS room was not accessible during the lamps' operation, by an Arduino Uno (rev. 3) microcontroller coupled to a relay module.

HFSS and radiative heat-flux map calibration

The 45 kW_{el} EPFL HFSS is a testing facility that delivers reproducible concentrated artificial light in a controlled laboratory environment. The HFSS comprises 18 × 2.5 kW_{el} identical short-arc xenon lamps coupled to a truncated ellipsoidal specular reflector arranged in two concentric circles.[38] The reflectors concentrate the light on the HFSS focal plane, where a maximum of 1–1.5 MW/m^2 peak flux per lamp is achievable. Lower radiative fluxes are obtained by out-of-focus positioning and by decreasing the power (i.e., by reducing the current) supplied to the lamps. The radiative fluxes were measured using a standardized procedure described by Levêque et al.[36] In this approach, a Lambertian target was observed by a CCD (charged-coupled device) camera (Basler scA 1400-17 gm, 1.5 MP, resolution 1,393 × 1,040, 12 bit pixel depth) equipped with a neutral density filter (Midwest ND400-55). The CCD camera was aligned in the HFSS axis and monitored gray-scale values of diffusely reflected radiative heat flux from the Lambertian target. We recorded gray-scale maps with the CCD camera by using 11 lamps on the outer ring with identical currents ranging from 80 to 100 A and for off-focal plane positions located 50 to 110 mm behind the focal plane. The gray-scale values were then calibrated with a heat-flux gauge (colloidal graphite coated, active area 1.82 mm^2, range 0–10 MW/m^2), which allowed the conversion of the gray-scale maps into calibrated radiative-heat-flux contour plots (Figure S8). The flux inhomogeneity (i.e., the difference between the maximum and the minimum flux normalized by the mean flux) and the averaged heat flux on a 1 cm^2 area (corresponding to the CPV module area) were quantified to identify the location with the least inhomogeneity for each radiative heat flux map. We identified six couples of HFSS current and CIPEC positions with inhomogeneities and irradiation concentrations between 15% and 41% and 101 and 518 kW/m^2, respectively.

Performance metrics

- Fill factor of the PV component: $FF = \frac{V_{mpp} I_{mpp}}{V_{oc} I_{sc}}$, where I_{mpp} is the current at maximum powerpoint, V_{mpp} is the voltage at maximum power point, I_{sc} is the short-circuit current, and V_{oc} is the open-circuit voltage of the PV.
- Inhomogeneity of the irradiation flux: $ih = \frac{C_{max} - Cmin}{Cmean}$, where C_{max} is the maximum concentration in the area of interest, C_{min} is the minimum concentration in the area of interest, and C_{mean} is the average concentration in the area of interest.
- Electrochemical (or EC operating) current density: $J_{ec} = \frac{I_{EC}}{A_{EC}}$, where I_{EC} is the operating current (in A) of the electrochemical component, and A_{EC} is the electrochemically active area (25 cm^2).
- PV (or PV operating) current density: $J_{PV} = \frac{I_{PV}}{A_{PV}}$, where I_{PV} is the operating current (in A) of the PV component, and A_{PV} is the active area of the PV component (0.96 cm^2).
- STH efficiency: $\eta_{STH} = \frac{I_{op}\ E_{eq}\ \eta_F}{P_{in}}$, where I_{op} is the operating current (A), η_F is the faradaic efficiency, E_{eq} (=1.229 V) is the equilibrium potential at standard

conditions, and P_{in} is the input power (W) to the device, which is calculated by the product of irradiation concentration (C); the incoming, non-concentrated light intensity (1,000 W/m^2); and the active area of the PV component (0.96 cm^2).

- RTE for stoichiometric operation: RTE = $\frac{V_{measured,FC}}{V_{measured,EC}}$ at each current density.
- Voltage efficiency of FC: $\frac{V_{measure,FC}}{1.48V}$.
- Stoichiometric molar hydrogen flow rate: $\dot{N}_{H2}\left[\frac{mol}{s}\right] = \frac{I\,[A]}{2F\left[s\frac{A}{mo}\right]}$.
- Stoichiometric volumetric hydrogen flow rate: $\dot{V}_{H2}\left[\frac{l}{min}\right] = 22.4\left[\frac{l}{mol}\right]\dot{N}_{H2}$.
- Pumping power to supply liquid water: $W = \frac{\rho g \Delta h Q}{\eta}$, where Q is the water volumetric flow rate, Δh is the head of the pump (~2 m) for the whole system (pipes, valves, etc.), and η is the efficiency of the pump (~0.75).
- Photo-driven electrolysis power output: $W_{H_2} = \dot{m}_{H_2} LHV$, where LHV = 33.33 kWh/kg and $\dot{m}_{H_2}$ is the converted hydrogen mass flow rate.

SUPPLEMENTAL INFORMATION

Supplemental information can be found online at https://doi.org/10.1016/j.xcrp.2024.101984.

ACKNOWLEDGMENTS

This work is supported by the ESA (ESA_AO9813 and ESA STAR AO 2-1799/21/NL/GLC/ov). We thank Brigitte Lamaze (ESA) for useful discussions, Vincent Python (EPFL) for helping in the automatization of the experimental setup, and Etienne Boutin (EPFL) for supporting the P-EC cell design.

AUTHOR CONTRIBUTIONS

Conceptualization, methodology, analysis, investigation, and writing—original draft, M.P. and A.C.; conceptualization, S.T.; investigation and analysis, M.J.; conceptualization, supervision, project administration, and writing—review &editing, S.H.

DECLARATION OF INTERESTS

The authors declare that there are no competing interests.

Received: November 7, 2023
Revised: March 18, 2024
Accepted: April 23, 2024
Published: May 17, 2024

REFERENCES

1. Shaner, M.R., Atwater, H.A., Lewis, N.S., and McFarland, E.W. (2016). A comparative technoeconomic analysis of renewable hydrogen production using solar energy. Energy Environ. Sci. *9*, 2354–2371. https://doi.org/10.1039/C5EE02573G.

2. Van de Krol, R., and Grätzel, M. (2011). Principles of Photoelectrochemical Cells. In Photoelectrochemical hydrogen production, R. van de Krol, ed. (Springer), pp. 13–67. https://doi.org/10.1007/978-1-4614-1380-6_2.

3. Ardo, S., Fernandez Rivas, D., Modestino, M.A., Schulze Greiving, V., Abdi, F.F., Alarcon Llado, E., Artero, V., Ayers, K., Battaglia, C., Becker, J.P., et al. (2018). Pathways to electrochemical solar-hydrogen technologies. Energy Environ. Sci. *11*, 2768–2783. https://doi.org/10.1039/c7ee03639f.

4. Haussener, S. (2022). Solar fuel processing: Comparative mini-review on research, technology development, and scaling. Sol. Energy *246*, 294–300. https://doi.org/10.1016/j.solener.2022.09.019.

5. Peharz, G., Dimroth, F., and Wittstadt, U. (2007). Solar hydrogen production by water splitting with a conversion efficiency of 18. Int. J. Hydrogen Energy *32*, 3248–3252. https://doi.org/10.1016/j.ijhydene.2007.04.036.

6. Tembhurne, S., Nandjou, F., and Haussener, S. (2019). A thermally synergistic photo-electrochemical hydrogen generator operating under concentrated solar irradiation. Nat. Energy *4*, 399–407. https://doi.org/10.1038/s41560-019-0373-7.

7. Holmes-Gentle, I., Tembhurne, S., Suter, C., and Haussener, S. (2023). Kilowatt-scale solar hydrogen production system using a concentrated integrated photoelectrochemical device. Nat. Energy *8*, 586–596. https://doi.org/10.1038/s41560-023-01247-2.

8. Tembhurne, S., and Haussener, S. (2016). Integrated Photo-Electrochemical Solar Fuel

Generators under Concentrated Irradiation. J. Electrochem. Soc. *163*, H999–H1007. https://doi.org/10.1149/2.0321610jes.

9. Regmi, Y.N., Peng, X., Fornaciari, J.C., Wei, M., Myers, D.J., Weber, A.Z., and Danilovic, N. (2020). A low temperature unitized regenerative fuel cell realizing 60% round trip efficiency and 10 000 cycles of durability for energy storage applications. Energy Environ. Sci. *13*, 2096–2105. https://doi.org/10.1039/c9ee03626a.

10. Mitlitsky, F., Myers, B., and Weisberg, A.H. (1998). Regenerative fuel cell systems. Energy Fuels *12*, 56–71. https://doi.org/10.1021/ef970151w.

11. Peng, X., Taie, Z., Liu, J., Zhang, Y., Peng, X., Regmi, Y.N., Fornaciari, J.C., Capuano, C., Binny, D., Kariuki, N.N., et al. (2020). Hierarchical electrode design of highly efficient and stable unitized regenerative fuel cells (URFCs) for long-term energy storage. Energy Environ. Sci. *13*, 4872–4881. https://doi.org/10.1039/d0ee03244a.

12. Sadhasivam, T., Dhanabalan, K., Roh, S.H., Kim, T.H., Park, K.W., Jung, S., Kurkuri, M.D., and Jung, H.Y. (2017). A comprehensive review on unitized regenerative fuel cells: Crucial challenges and developments. Int. J. Hydrogen Energy *42*, 4415–4433. https://doi.org/10.1016/j.ijhydene.2016.10.140.

13. Lim, B., Jiang, M., Camargo, P.H.C., Cho, E.C., Tao, J., Lu, X., Zhu, Y., and Xia, Y. (2009). Pd-Pt bimetallic nanodendrites with high activity for oxygen reduction. Science *324*, 1302–1305. https://doi.org/10.1126/science.1170377.

14. McCrory, C.C.L., Jung, S., Ferrer, I.M., Chatman, S.M., Peters, J.C., and Jaramillo, T.F. (2015). Benchmarking Hydrogen Evolving Reaction and Oxygen Evolving Reaction Electrocatalysts for Solar Water Splitting Devices. J. Am. Chem. Soc. *137*, 4347–4357. https://doi.org/10.1021/ja510442p.

15. McCrory, C.C.L., Jung, S., Peters, J.C., and Jaramillo, T.F. (2013). Benchmarking Heterogeneous Electrocatalysts for the Oxygen Evolution Reaction. J. Am. Chem. Soc. *135*, 16977–16987. https://doi.org/10.1021/ja407115p.

16. Jung, H.-Y., Park, S., and Popov, B.N. (2009). Electrochemical studies of an unsupported PtIr electrocatalyst as a bifunctional oxygen electrode in a unitized regenerative fuel cell. J. Power Sources *191*, 357–361. https://doi.org/10.1016/j.jpowsour.2009.02.060.

17. Yim, S.-D., Lee, W.-Y., Yoon, Y.-G., Sohn, Y.-J., Park, G.-G., Yang, T.-H., and Kim, C.-S. (2004). Optimization of bifunctional electrocatalyst for PEM unitized regenerative fuel cell. Electrochim. Acta *50*, 713–718. https://doi.org/10.1016/j.electacta.2004.02.068.

18. Ioroi, T., Kitazawa, N., Yasuda, K., Yamamoto, Y., and Takenaka, H. (2000). Iridium Oxide/Platinum Electrocatalysts for Unitized Regenerative Polymer Electrolyte Fuel Cells. J. Electrochem. Soc. *147*, 2018–2022. https://doi.org/10.1149/1.1393478.

19. Dumortier, M., Tembhurne, S., and Haussener, S. (2015). Holistic design guidelines for solar hydrogen production by photo-electrochemical routes. Energy Environ. Sci. *8*, 3614–3628. https://doi.org/10.1039/c5ee01821h.

20. Cruz, J.C., Baglio, V., Siracusano, S., Ornelas, R., Ortiz-Frade, L., Arriaga, L.G., Antonucci, V., and Aricò, A.S. (2011). Nanosized IrO_2 electrocatalysts for oxygen evolution reaction in an SPE electrolyzer. J. Nanoparticle Res. *13*, 1639–1646. https://doi.org/10.1007/s11051-010-9917-2.

21. Kerkoub, Y., Benzaoui, A., Haddad, F., and Ziari, Y.K. (2018). Channel to rib width ratio influence with various flow field designs on performance of PEM fuel cell. Energy Convers. Manag. *174*, 260–275. https://doi.org/10.1016/j.enconman.2018.08.041.

22. Zhou, H., Chen, B., Meng, K., Luo, M., Li, P., and Tu, Z. (2022). Combination effect of flow channel configuration and anode GDL porosity on mass transfer and performance of PEM water electrolyzers. Sustain. Energy Fuels *6*, 3944–3960. https://doi.org/10.1039/D2SE00974A.

23. Carmo, M., Fritz, D.L., Mergel, J., and Stolten, D. (2013). A comprehensive review on PEM water electrolysis. Int. J. Hydrogen Energy *38*, 4901–4934. https://doi.org/10.1016/j.ijhydene.2013.01.151.

24. Hwang, C.M., Ishida, M., Ito, H., Maeda, T., Nakano, A., Kato, A., and Yoshida, T. (2012). Effect of titanium powder loading in gas diffusion layer of a polymer electrolyte unitized reversible fuel cell. J. Power Sources *202*, 108–113. https://doi.org/10.1016/j.jpowsour.2011.11.041.

25. Vincent, I., Lee, E.C., and Kim, H.M. (2020). Solutions to the water flooding problem for unitized regenerative fuel cells: status and perspectives. RSC Adv. *10*, 16844–16860. https://doi.org/10.1039/D0RA00434K.

26. Chen, W., Chen, B., Meng, K., Zhou, H., and Tu, Z. (2023). Experimental study on dynamic response characteristics and performance degradation mechanism of hydrogen-oxygen PEMFC during loading. Int. J. Hydrogen Energy *48*, 4800–4811. https://doi.org/10.1016/j.ijhydene.2022.11.036.

27. Cho, J., Kim, H.S., and Min, K. (2008). Transient response of a unit proton-exchange membrane fuel cell under various operating conditions. J. Power Sources *185*, 118–128. https://doi.org/10.1016/j.jpowsour.2008.06.073.

28. Halalay, I.C., Swathirajan, S., Merzougui, B., Balogh, M.P., Garabedian, G.C., and Carpenter, M.K. (2011). Anode Materials for Mitigating Hydrogen Starvation Effects in PEM Fuel Cells. J. Electrochem. Soc. *158*, B313. https://doi.org/10.1149/1.3530796.

29. Lim, K.H., Lee, W.H., Jeong, Y., and Kim, H. (2017). Analysis of Carbon Corrosion in Anode under Fuel Starvation Using On-Line Mass Spectrometry in Polymer Electrolyte Membrane Fuel Cells. J. Electrochem. Soc. *164*, F1580–F1586. https://doi.org/10.1149/2.0731714jes.

30. Li, W., Tian, H., Ma, L., Wang, Y., Liu, X., and Gao, X. (2022). Low-temperature water electrolysis: fundamentals, progress, and new strategies. Mat. Adv *3*, 5598–5644. https://doi.org/10.1039/D2MA00185C.

31. Hwang, C.M., Ishida, M., Ito, H., Maeda, T., Nakano, A., Hasegawa, Y., Yokoi, N., Kato, A., and Yoshida, T. (2011). Influence of properties of gas diffusion layers on the performance of polymer electrolyte-based unitized reversible fuel cells. Int. J. Hydrogen Energy *36*, 1740–1753. https://doi.org/10.1016/j.ijhydene.2010.10.091.

32. Ioroi, T., Oku, T., Yasuda, K., Kumagai, N., and Miyazaki, Y. (2003). Influence of PTFE coating on gas diffusion backing for unitized regenerative polymer electrolyte fuel cells. J. Power Sources *124*, 385–389. https://doi.org/10.1016/S0378-7753(03)00795-X.

33. Lee, J., Yip, R., Antonacci, P., Ge, N., Kotaka, T., Tabuchi, Y., and Bazylak, A. (2015). Synchrotron investigation of microporous layer thickness on liquid water distribution in a PEM fuel cell. J. Electrochem. Soc. *162*, F669–F676. https://iopscience.iop.org/article/10.1149/2.0221507jes.

34. Pellow, M.A., Emmott, C.J.M., Barnhart, C.J., and Benson, S.M. (2015). Hydrogen or batteries for grid storage? A net energy analysis. Energy Environ. Sci. *8*, 1938–1952. https://doi.org/10.1039/c4ee04041d.

35. Ito, H., Iwamura, T., Someya, S., Munakata, T., Nakano, A., Heo, Y., Ishida, M., Nakajima, H., and Kitahara, T. (2016). Effect of through-plane polytetrafluoroethylene distribution in gas diffusion layers on performance of proton exchange membrane fuel cells. J. Power Sources *306*, 289–299. https://doi.org/10.1016/j.jpowsour.2015.12.020.

36. Levêque, G., Bader, R., Lipiński, W., and Haussener, S. (2016). Experimental and numerical characterization of a new 45 kWel multisource high-flux solar simulator. Opt Express *24*, A1360–A1373. https://doi.org/10.1364/OE.24.0A1360.

37. Boutin, E., Patel, M., Kecsenovity, E., Suter, S., Janáky, C., and Haussener, S. (2022). Photo-Electrochemical Conversion of CO2 Under Concentrated Sunlight Enables Combination of High Reaction Rate and Efficiency. Adv. Energy Mater. *12*, 2200585. https://doi.org/10.1002/aenm.202200585.

38. Bader, R., Haussener, S., and Lipiński, W. (2014). Optical Design of Multisource High-Flux Solar Simulators. J. Sol. Energy Eng. *137*, 021012. https://doi.org/10.1115/1.4028702.